Title

Volumetric data analysis enabled spatially resolved optoretinogram to measure the functional signals in the living retina

Journal

Journal of Biophotonics, 15(3)

ISSN

1864-063X

Authors

Zhang, Lijie
Dong, Rongyao
Zawadzki, Robert J
et al.

Publication Date

2022-03-01

DOI

10.1002/jbio.202100252

Peer reviewed

HHS Public Access

Author manuscript

J Biophotonics. Author manuscript; available in PMC 2023 March 01.

Published in final edited form as:

J Biophotonics. 2022 March ; 15(3): e202100252. doi:10.1002/jbio.202100252.

Volumetric data analysis enabled spatially resolved optoretinogram to measure the functional signals in the living retina

Lijie Zhang[1], **Rongyao Dong**[1], **Robert J. Zawadzki**[2,3], **Pengfei Zhang**[1,2,*]

[1]School of Optoelectronic Engineering and Instrumentation Science, Dalian University of Technology, 116024, China

[2]UC Davis Eye-Pod Small Animals Ocular Imaging Laboratory, Department of Cell Biology and Human Anatomy, University of California Davis, Davis, California, 95616, United States

[3]UC Davis Eye Center, Department of Ophthalmology & Vision Science, University of California Davis, Sacramento, California, 95817, United States

Abstract

Optoretinogram, a technique in which optical coherence tomography (OCT) is used to measure retinal functions in response to a visible light stimulus, can be a potentially useful tool to quantify retinal health alterations. Existing experimental studies on animals have focused on measuring the global retinal response by transversally averaging 3D data across the retina, which minimizes the spatial resolution of the signals, and limits the signal-to-noise ratio (SNR) because only central B-scans are collected and analyzed. These problems were addressed in this study by collecting volumetric data to probe functional signals and developing an improved 3D registration approach to align such series-acquired OCT volumes. These data were then divided into small blocks and subject to a spatiotemporal analysis, whose results confirmed the spatial-dependence of functional signals. By further averaging, the overall measurement accuracy for position and scattering signals was estimated to be approximately 30 nm and 1.1%, respectively. With improved accuracy, this method revealed certain novel functional signals that have not been previously reported. In conclusion, this work provides a powerful tool to monitor retinal local and global functional changes in aging, diseased, or treated rodent eyes.

Graphical Abstract

*Correspondence: Pengfei Zhang, Dalian University of Technology, 116024, China, pfzhang@dlut.edu.cn.

AUTHOR CONTRIBUTIONS

L.Z. was involved in developing the automated code and software for layer segmentation, and data analysis and R. D worked on data processing, while R.J.Z was contributed to the conceptualization, data interpretation and writing. P.Z. was involved in conceptualization, data analysis, writing, and project management.

CONFLICT OF INTEREST

The authors declare no financial or commercial conflict of interest.

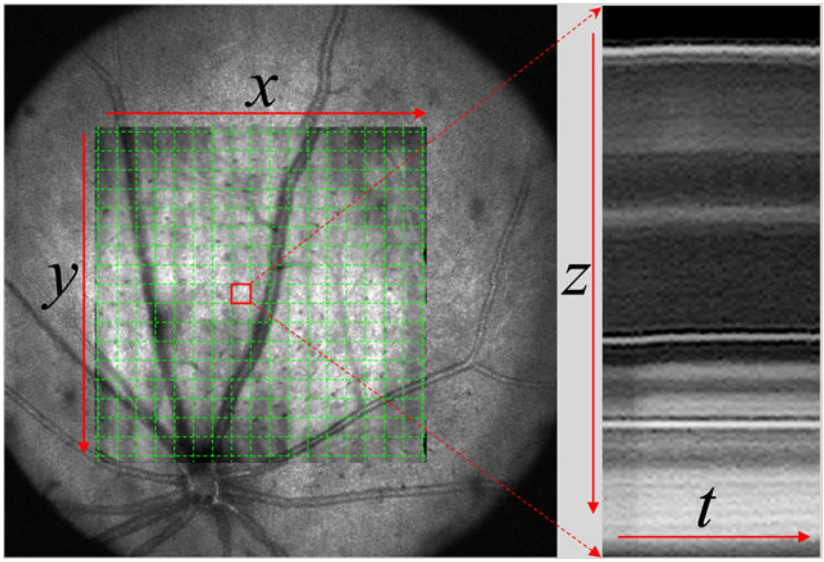

Opto-retinogram (ORG) is a new imaging technique for probing the opto-physiological signals arising from phototransduction. It can precisely measure μm-order photoreceptor elongation and 3~5-fold OCT backscattering changes induced by visible light bleach with wide-field OCT in the mouse eye. By further dividing the 3D data into small blocks, each block can be temporally analyzed and quantified, thus enabling spatially-resolved 4D ORG to monitor the functional changes of the living retina.

Keywords

optical coherence tomography; functional imaging; *in vivo* imaging; mouse retina; optoretinogram

1 INTRODUCTION

The primary function of the retina is to capture the photons of visible light and generate visual electrophysiological signals for transmission to the brain to form the vision[1]. The incidence of light on the retina induces not only biochemical reactions, but also various other changes in its optical properties, such as rod membrane structures and near-infrared transmission[2, 3]. Therefore, the development of non-invasive, spatially resolved methods for an all-optical detection of the living retina's function is of great significance because it may not only provide new insights into the underlying physiology, but more importantly, it may also become a new diagnostic tool for various retinal diseases. Optical coherence tomography (OCT) is a non-invasive imaging modality that has many successful applications in both fundamental and clinical ophthalmology[4]. It typically utilizes low-coherence, near-infrared (NIR) light to measure the interference signal between the back-reflected light from the sample and the reference mirror; by combining 2D scanning with a Fourier transformation of the spectral fringe, it reconstructs a 3D volumetric image of the scattering microstructures inside the sample. In principle, NIR-OCT offers unique advantages in probing retinal response to a visible-light stimulus, due to its high axial resolution (typically a few micrometers) for precisely localizing the signal and the use

of NIR light to minimize undesired photo-stimulation. Therefore, for the last 15 years, scientists have been using OCT to investigate retinal functional responses induced by visible-light stimuli[5–9].

Early studies focused on examining the changes in the intensities of backscattered light[10]. However, the signals generated therein were not very convincing because of the small difference in intensity from before and after exposure to light stimulus and the low signal-to-noise ratio (SNR), especially for human imaging often disturbed by rapid eye movements. Alternative image analysis methods could provide higher SNR functional signals, for example, by calculating the dynamic differentiation of intensity images recorded at pre- and post-stimulus periods[11, 12]. Later, a breakthrough in the measurement of optical path changes in the range of a few tens to a few hundreds of nanometers, representing the length changes of the cone outer segment (OS) was first demonstrated by D. Hillmann et. al in a phase-resolved, full-field OCT system[13, 14], following which it was soon applied to raster point-scan[15–17] and line-scan[18–20] OCT systems. Phase-resolved approaches for measuring optical path changes provide the utmost precision, which is sufficient for identifying different classes of cones even at the cellular level[16, 18]. However, the functional signals in these studies were typically obtained using adaptive-optics-enhanced imaging systems, in which the field-of-view (FOV) is small owing to the demand for high lateral resolution. Thus, their application to routine screening (in which large FOV is often required) remains limited. In contrast, although intensity-[21], and phase-based analyses[22] using large-FOV imaging systems can probe the overall retina response with high sensitivity after spatial averaging, they have not demonstrated a spatially resolved capability to detect local abnormalities in retinal function.

Two types of functional signals - back-scattering and photoreceptor elongations - were reported using large-FOV, point-scan OCT for mice in our previous study[23], which helped explain the underlying physiological mechanism of the signals. However, it focused on extracting the global retinal response without spatial resolution, and the SNR of the signals was limited, given that only a few central B-scans were used for data analysis. Since random measurement errors can be effectively reduced by averaging more datasets, volumetric data acquisition and analysis were used to develop the spatially-resolved capability of the OCT functional imaging. The use and averaging of more data in the signal extraction allowed for a further suppression of random errors in measurement[24], thus increasing the SNR. Volumetric data averaging can greatly increase OCT image quality to aid in the visualization of highly transparent cells in the inner retina of both humans[25, 26] and rodents[27, 28]. The key to successful volumetric averaging is the precise registration of 3D images between series datasets. Hence, we extended the 3D registration to align the time-series OCT volumes before and after exposure to visible-light stimulus and then extracted the functional signals in both temporal and spatial capacities (Section 2). As demonstrated below, this not only enabled the spatially-resolved capability of large-FOV functional imaging (which, by itself, could be very important in measuring local disorders of the retina, such as light-induced retinal damage[29]), but also greatly increased the SNR of the overall retina response signal, which led to the discovery of a few new functional signals (Section 3).

2 Materials and Methods

2.1 Experimental setup and data acquisition protocol

The data were acquired using a custom-built, multimodal retinal imaging system, the details of which are described in our previous work[30]. A brief overview of the system is given here: it combines two imaging modalities - scanning laser ophthalmoscopy (SLO) and OCT - via a dichroic mirror (DM) and shares the same scanning system between them. The SLO is equipped with a triggerable, 488-nm light source (Coherent, 488–30FP) for stimulus light delivery to bleach the rhodopsin of the retina[31]. In the meantime, it can also capture a small portion of the OCT light reflected by the DM to form the fundus images (Figure 1 (a), top row). Because the stimulation was delivered to the eye via the SLO through a point-by-point scanning, where each scan point has the same light intensity, the stimulus has a uniform distribution (4.7 μW over ~35° of FOV). The duration of the stimulation was equal to that of a single SLO scan (~1.47 s, 408 pixels × 360 pixels × 10 μs pixel dwell time, note that there are 48 pixels in the 408 pixels as the scanning fly-back points). The bleaching was intended to be delivered at the 40th SLO scan and its level was set to 10%, this was performed to saturate the retinal photoreceptor swelling response and provide a strong scattering response[23]. The OCT used an 860nm superluminescent diode (SLD, T-860-HP, Superlum) light source with an effective full-width-at-half-maximum (FWHM) bandwidth of ~ 82 nm, which was synchronized to the third of every five SLO scans (Figure 1(a)). The overall retinal response obtained by averaging the SLO frames is shown in Figure 1(b), which clearly indicates not only an increase in the retinal scattering intensity after the delivery of the bleaching flash, but also the time point at which the flash was delivered (indicated by the outlier in the scattering plot in Figure 1 (b) and by the cyan-colored, thunderbolt-shaped marker throughout Figure 1(a–d)). Similarly, the overall retinal response generated by averaging OCT volumes is shown in Figure 1 (c). The system was running at a pixel-dwell / A-scan rate of 100kHz, allowing simultaneous SLO/OCT data acquisition. The timestamp of each SLO and OCT dataset was recorded for cross-validation, and the time intervals between the SLO frames and the OCT volumes were about 1.73 s and 8.67 s, respectively (Figure 1(d)).

2.2 Volumetric data processing and automated layer extraction

Data acquisition through the optoretinogram (ORG) generated 250 SLO frames and 50 OCT volumes for each measurement, as the input of data post-processing shown in Figure 2. Each OCT volume had an FOV of ~35 ° (which translates to ~1.4 mm on the retina) throughout 360 × 360 A-scans, giving an A-scan spacing of approximately 3.9 μm. The key to volumetric data analysis is 3D registration. A method for the volumetric registration of standard 3D OCT datasets without bleaching was developed in our previous work[27]. However, because of the changes in the intensity of the overall *enface* OCT projection before and after bleaching, the framework did not work well in aligning the *enface* time-series images; therefore, the layers were automatically segmented to extract the *enface* projections of the data from the outer plexiform layer (OPL) to the nerve fiber layer (NFL) by calculating and compensating for the overall axial shifts between volumes. All subsequent steps of the 3D registration were identical to the same procedure described in our previous work[27]. The aligned volumes were divided into M × N blocks containing 20

× 20 A-scans in each block, corresponding to an area of 78 μm × 78μm. The A-scans in each block were further cross-correlated, averaged, and then deconvoluted using the blind deconvolution algorithm (described in section 2.3) with the estimated axial point-spread-function (PSF, FWHM = 3.6μm) as the initial input. These deconvoluted A-scans from each block, along with the time series, were automatically aligned to the Bruch's membrane (BrM). The peak position and intensity of nine layers from BrM to the NFL were automatically identified and extracted from the datasets (as described below) for further modeling with a second-order system (described in Section 2.4).

The process involved in automatic peak detection can be divided into the following three steps:

1. Identifying the scattering peaks on the averaged A-scan within the center block (for volume #1). Since the center block usually had the best image quality, it was the first to be processed. By calculating the axial gradient of the OCT line profile and determining its maximum and minimum values, we were able to confidently determine the BrM location, after which the intensity peaks of the other retinal layers could be readily identified with preset parameters defining the position ranges of each peak.
2. Identifying the intensity peaks for the rest of the blocks (for volume #1): Once the above step was performed, the software then used the peak locations of the center block as the baseline input and searched for the peak locations of the adjacent blocks. This search was conducted in a ring-by-ring fashion (the rings are defined by the red, dashed rectangles and lines with arrowheads as shown in Figure 2), from the inner ring to the outer ring. It involved calculating the maximum and minimum values of axial gradient to identify the BrM, while assuming that there was no big jump in the peak locations of adjacent blocks.
3. Identifying the peaks of the blocks in consecutive volumes (for volume #2 - #50): Once the above two steps were performed, the software then searched the peak locations in the time-series datasets. Given the relatively minor changes in the peak locations between adjacent time-series scans (less than one micrometer), the peak locations within this range were searched, following which all the data were aligned into BrM. After this, the peak locations and intensities were finally obtained.

2.3 Blind deconvolution algorithm and spatially-dependent PSF recovery

If the calibration and dispersion compensation of the spectral signal are accurate, the axial resolution of OCT imaging depends on the spectrum of the OCT source (i.e., on its central wavelength and effective bandwidth). Given that the scanning beam may pass through a different portion of the system optics and ocular pupil due to beam scanning and pupil wonder[33], this may introduce minor chromatic aberrations that affects the axial PSF. Therefore, a blind deconvolution algorithm and the estimated global axial PSF were used to deconvolute axial profiles across different blocks to sharpen the A-line profiles. Although a fixed PSF would also work for this purpose to some extend[32], the blind deconvolution approach is more accurate. The details are as follows:

Deconvolution was necessary to reveal the apical surface of the retinal pigment epithelium (RPE) and rod outer segment tips (ROST) from the averaged A-scan axial profile[32]; however, a fixed PSF was used without considering the chromatic aberration mentioned above. To solve this problem, a blind deconvolution algorithm was employed in this study by using the 'deconvblind' function in MATLAB™ to simultaneously restore the image and the axial PSF (in Gaussian shape) with an iterative process. In short, blind deconvolution enables the recovery of a sharp version of a blurry input image when the blur kernel is unknown[34]. The algorithm maximizes the likelihood that the deblurred image, when convolved with the recovered PSF, is an instance of the input blurry image, assuming a Poisson distribution of noise. The blind deconvolution algorithm can be effectively used when information on distortion is unknown. Here, both the averaged line profile and the PSF are one-dimensional data, whereas the kymogram is a spatial time-series line profiles, whose initial input is the estimated PSF; the algorithm could satisfactorily recover both the deblurred kymograph and the PSF.

To deblur the line profiles, the OCT volume data were first segmented into small blocks, as shown by the green lattice in Figure 3 (a). These data were divided into 17 × 17 blocks, and the 20 × 20 A-scans in each block were aligned and averaged according to the procedure shown in Figure 2. The blind deconvolution algorithm was then carried out by applying the 'deconvblind' function in MATLAB™ to each block to estimate the axial PSF; its result are shown in Figure 3 (b). Interestingly, the axial PSF and the *enface* image quality (which is related to the transverse PSF) have a good correlation with each other - one can find that axial PSFs corresponding to the blurred parts of the image (e.g., the upper two corners) have larger FWHM of PSF, while the axial PSF in the center, where the image was sharper, is smaller. This can be explained by field-dependent ocular aberrations or imaging-beam wandering in the pupil plane of the scanning system[33]. Because the wavefront aberration is dependent on both the imaging-field of the retina and entrance-pupil-position of the mouse ocular, each scan probed the retina with slightly different aberrations, which caused the differences among the transverse and axial PSFs in each block. To test the reliability of the deconvolution, a simulation with 50 deconvolutions was carried out; their results had an average standard deviation of 0.085 μm, which was approximately 2.7 % of the mean value of the recovered axial PSF (3.1 μm).

Further examinations of the kymograms showed that they became sharper after deconvolution (Figure 3 (c) and (d)); more importantly, the dip between OS Tips and RPE (indicated by the green arrow in Figure 3 (d)) was more visible after deconvolution, further proving that the upper scattering intensity peak corresponds to the OS Tips, while the lower scattering peak is the apical side of the RPE (magenta arrow in Figure 3 (e))[32]. Two additional lamina bandings (dark/bright) were observed in the outer retina, right next to the external limiting membrane (ELM). The upper banding was barely visible in the raw, log-scale OCT signal, while the lower one was invisible; this could be an artifact of the deconvolution process. Nevertheless, given its small amplitude, it might have had only a negligible effect on the major finding of the dark band between the OS tips and the apical RPE. Figure 3 (e) compared the raw and deconvoluted line profiles, the blind deconvolution algorithm did not significantly alter pixel intensities in most of the line profile, but did increase the pixel intensities for a few bands (notably, for the NFL, ELM,

and BrM peaks); consequently, the valley intensities adjacent to these peaks were decreased. Thus, the algorithm did not significantly alter intensities in the *enface* plane for most parts of the retina, but did increase them for the 'peaks' and decrease them for the 'valleys'.

2.4 Estimating the transfer function with a second-order system model

In the model of our previous work[23], the position changes were fitted to the Lambert *W* function, which considered only the rising part of the signal but neglected its falling part. The signal was reconsidered from the perspective of control engineering. In control theory, signal transfer, for example, from the input visible light stimulus to an output retina elongation/scattering response, is often governed by a certain system transfer function. Taking the retinal elongation as an example, for instance, the retina has two different and independent types of energy storage during the ORG response, one is tissue tension (e.g. ELM as a tight junction), while the other is the resistance from the surrounding tissue. This is similar to the spring and the inert mass in a typical spring-mass-damper system; therefore, we modeled retinal response as a second-order system, which can be described by its transfer function. The Laplace transform provides a convenient and powerful approach for such systems. Given a system with time-dependent input $u(t)$ and output $y(t)$, as shown in Fig. 2, its response to any disturbance may be completely characterized by knowing either the impulse response $h(t)$ or its Laplace transform, with a assumed transfer function of $H(s) = Y(s)/U(s)$. The flash-stimulus input can be treated as an impulse function, defined as:

$$\delta_t = \begin{cases} 1, \ if \ t = 0 \\ 0, \ if \ t \neq 0 \end{cases} \tag{1}$$

As stated above, the impulse response, $h(t)$, defines the response of a system. Its transfer function can be described in the root-locus form as follows:

$$\mathrm{H(s)} = \frac{b_m s^m + b_{m-1} s^{m-1} + \cdots + b_0}{s^n + a_{n-1} s^{n-1} + \cdots + a_0} \tag{2}$$

where $b_0 \cdots b_m (m \leq$ for a second – order system) are the coefficients of the numerator, and the roots of the polynomial are called the 'zeros' of H(s); while $a_0 \cdots a_{n-1} (n = 2$ for a second – order system) are the coefficients of the denominator, and the roots of the polynomial are called the 'poles' of H(s).

2.5 Animals preparations and imaging

All mouse husbandry and handling protocols were approved by the University of California's Institutional Animal Care and Use Committee (IACUC), which strictly adheres to all guidelines of the NIH and satisfies those of the Association for Research in Vision and Ophthalmology for animal use. B6-albinos (B6(Cg)-Tyrc-2J/J) mice are congenic with B6 mice (C57BL/6(J)), save for the null mutation in the tyrosinase gene that eliminates melanin. Since the lack of melanin in albino mice allows for the clear visualization of ROST and BrM, only the B6-albino mice were used in this study. However, the methodology developed here should be applicable to B6 mice as well. Adult B6 albino mice, aged two months, were obtained from the Jackson Laboratory and maintained on a 12:12, ~100-lux light cycle.

Before the experiments, the mice were dark-adapted overnight to enable the completely adaption of their eyes to the darkness. During measurements, they were anesthetized with inhalational isoflurane (2–2.5% in O_2), and their pupils were dilated with medical-grade tropicamide and phenylephrine. A contact lens and gel (GelTeal Tears, Alcon, USA) were used to maintain good tear film quality and corneal transparency during *in vivo* retinal imaging[35]. Their superior retinas were imaged with an FOV of approximately 35°.

3 RESULTS

3.1 Spatially-resolved functional ORG signals

The functional ORG signals for each block were extracted from the processed data. As shown in our previous studies[23, 32], multiple ORG signals (such as peak scattering intensity changes from ISOS, OS tips, RPE, BRM, and Choroid; along with the peak location shifts from all seven layers with respect to BrM defined in Figure 3) can be identified. Among them, three signals were the most distinguishable: one was the ELM peak position shift, while the other two were the ISOS peak position and scattering intensity changes. Therefore, these three signals were used to demonstrate the spatial characteristics of the functional signals.

The ELM peak shift with respect to BrM was first extracted and then evaluated; here, a positive shift indicated that the ELM was shifting away from BrM, while a negative shift denoted an ELM moving closer to the BrM. The *enface* display and 3D visualization are shown in Figure 4 (a) and 4 (b), respectively. It can be seen that, the ELM peak position changes (Figure 4 (c)) ranged between 1–3 μm, with the largest changes in the middle and the smallest ones at the edge. One possible reason for this ‘hat’ shaped distribution could be following: because the ELM is composed of a strong, tightly-held, cohesive structure across the retina[36], we hypothesized that when the ELM in the bleached region was shifted away from the BrM (due to the osmotic pressure generated by the bleaching), there was no osmotic pressure on the area surrounding the bleached region, thus the ELM outside the bleached region tended to stay at its original position; However, these two ELM regions (the bleached area and its surroundings) were physically connected and the resistance from the surrounding tissue reduced the ELM changes at the edge of the bleached region, which caused the ‘hat’ shaped of distribution of the ELM peak position changes.

The retinal response to the light stimulation can depend on many factors, including the energy distribution of the stimuli and the aberrations in the ocular and imaging systems. These factors may also contribute to the final measurement of the ORG signal. In our experiment, the bleaching light was delivered by the scanning system, ensuring each point had the same power and pixel dwell time; therefore, theoretically, the stimuli had a uniform energy distribution. Given that the scanning beam passed through a different portion of the system and ocular optics due to scanning and beam wonder on the pupil, the ocular and system aberrations of the imaging system might also affect the ‘hat’ shaped distribution of the response. Considering the small size of the imaging beam (~0.5 mm) used in our system[37], these aberrations were minor, and this was proven by the variation of the deconvoluted PSF (~±8 %). In contrast, the variation in the ELM position shift, shown by the ‘hat’ shaped distribution was ~±43 %. Therefore, the ‘hat’ shaped signal response should

be largely caused by the local mechanical property of the retina itself, rather than by the factors described above.

The axial locations of the ELM peaks in individual blocks, shown in Figure 4 (a), were extracted and plotted as shown in Figure 4 (c); they were a bit noisy, with a tendency to have smaller variance in the beginning and larger variance at the end. After row-by-row averaging, the ORG response lines were smoother and had the same tendency of signal variance. As discussed in the above paragraph, signal variance in the second half was due to differences in location (signal amplitude was larger in the middle and smaller at the edge). At the beginning, however, when the ELM in the bleached region can move more freely with less resistance from its surroundings, the signal from all the blocks increased at a similar speed (same slope, indicated by the red dashed line in Figure 4 (d)).

The averaged ORG signal from all the blocks is shown in Figure 4 (e). As expected, it was much smoother than the raw data, thus can be well described by a second-order system. The data were fitted by the transfer function estimated from Equation (2), as shown by the red line. The standard deviation of the difference between the ground average and its fitted data was calculated to be 27nm as the estimated measurement error. This fitting was further applied to calculate the standard error of the data in Figure 4 (c) and 4 (d), where it was found to be inversely proportional to the square root of the number of averaged blocks (N). As an estimation of the measuring error for our previous protocol[23], it roughly equals the standard error of row-by-row averaging (N = 17) which is ~120 nm. Therefore, the volumetric data acquisition and analysis yielded a signal that was ~4 – 5 times better than the one yielded by our previous approach.

As the other two representative functional signals, the 2D and 3D display of the maximum location and scattering changes from the individual blocks of ISOS were extracted and displayed in Figure 5 (a, d) and 5 (b, e), respectively. The location changes predominantly ranged from 1–2 μm. ISOS peak position changes were marginally smaller than the ELM position shifts (Figure 4 (a) and 4 (b)), more importantly, were less ‘hat’ shaped and had a larger variance, which might indicate that the connections between the ISOS structures and their surroundings were much weaker than the corresponding connection of the ELM. The ISOS scattering signals were normalized to their baseline intensity before bleaching, with the ratio largely ranging from 2 to 5. First, the scattering changes did not seem to correlate with the peak location changes (Figure 5 (a) and (d)), the variance of the scattering signal might be due to differences in the baseline refraction index within the rod’s population for the dark-adapted retina. The ground average of the ISOS scattering signal was further rescaled to [0, 1], as shown in Figure 5 (f). Its dynamics can also be described by a second-order system and the fitting simulation is displayed in the form of red curves. The standard error difference between the measured ‘Ground Average’ data and the fitted ‘Simulation’ data was calculated to be 1.12%; this was the estimated measurement accuracy for the scattering signal using the volumetric data analysis method.

3.2 Discovery of new functional signals in volumetric data analysis

With the improved measurement accuracy, we re-evaluated all the retinal ORG signals, and found several new scattering changes that were not identified in our previous studies.

A representative kymogram, plotted on a logarithmic scale and by averaging five blocks in the center of the image, is shown in Figure 6 (a). In total, 10 scattering retinal layers/bands were identified from the kymograph. The signals from the outer retina, including NFL, IPL, INL, OPL, and ONL, were displayed in Figure 6 (b) and the signal from the IPL is the most notable amongst them due to an evident increase in scattering right after the bleaching. Light-induced responses were also likely evoked from the INL, OPL, and the ONL, as indicated by the scattering changes right after the bleaching. In contrast, the scattering changes from the NFL were most likely noise. The signals from the inner retina, including ELM, ISOS, OS tips, RPE, and BrM, were displayed in Figure 6 (c) and the scattering signals from ISOS to BrM were all clearly visible after the bleaching. We also noticed a minor rise in intensity for the ELM right after the bleaching; the random variations of this signal after 50 s, however, made it unconvincing. While there might be a fast signal (within the first 10s) for ELM scattering changes, a much higher temporal sampling rate would be required to resolve it. Due to the limited temporal sampling of our system (~0.12 Hz), it was only those ORG signals with frequencies lower than ~0.06Hz that could be reliably measured. It was also noted that the signals from several layers showed a decreasing trend even before stimulation. We suspect that this could be caused by the isoflurane anesthesia used in the experiments. As shown in previous studies, anesthesia can affect retinal blood flow[38], intraocular pressure (IOP)[39, 40], and the functional electrical activities measured by the electroretinogram (ERG)[41]. It is, thus, possible that anesthesia also affects the retinal scattering and the functional optical signals measured by ORG in this study. To investigate this hypothesis, detailed experiments comparing the ORG responses in awake and anesthetized mice will need to be conducted in the future.

To check the reproducibility of the ORG signals identified above across different mice, we imaged five mice eyes and extracted the scattering ratio changes for IPL, as shown in Figure 7 (a); surprisingly, this signal had a high variation across the mice. Two out of five showed notable IPL scattering changes, while the other three cases showed minute scattering increases in the post-bleaching IPL intensity. IPL consists of synaptic connections between the axons of bipolar and amacrine cells and the dendrites of ganglion cells[42], enclosed by dense capillaries. The source of this signal is probably associated with a light-evoked activation of the inner retinal neurons and a corresponding increase in the local blood flow[43]. In contrast, there was a robust decrease in intensity for the ONL (Figure 7 (b)), averaging at nearly 10% of the maximum change. Similarly, it was also a slow response (~100s), which is possibly related to the water movement and homeostatic rebalance of the retinal fluid[44] in the ONL after the visible light stimulus.

With the high SNR scattering signals and fitting, the timing of the signal changes was further examined, as shown in Figure 7 (c). Three scattering signals, including ISOS, OS tips, and apical RPE were rescaled to [0, 1], and their fit with a second-order system was plotted for comparison. Two types of timing parameters – one when the signal started (t_0) after bleaching, and the other refer to the speed at which the signal reached the value corresponding to 90% of its maximum value (t_{90}), were extracted, as shown in Table 1. On average, the ISOS scattering signal started first at 0.48 s after the bleaching, followed by the OS tips (0.58 s), and then the PRE signal (1.73 s); this confirmed the ISOS signal to be the

driving force for all the ORG changes. The order of the t_{90} values of these signals, however, was reversed, being 36.6, 52.4 and 56.6 s for apical RPE, OS tips and ISOS, respectively.

Fitting precision can be affected by system/imaging noises and the relatively low temporal sampling (~8.67 s). To study this, we simulated a noisy situation by adding 10× white noise to the data; its results are shown in Table 1. On average, as expected, the increased noise affected t_0, while the values of t_{90} were maintained. However, we admit that there is not a good way to simulate a higher temporal resolution, and plan to check it more carefully when the data acquisition speed is improved in the future. Overall, given its smaller value, t_0 was more sensitive to the noise and low temporal resolution; while t_{90} was more robust, given its relatively large value compared to the sampling. A higher sampling rate would help improve the temporal precision of the fitting.

4. Discussion

4.1 Comparison of the global retinal scattering signals in response to the visible light stimulus measured by SLO and OCT

Five mouse eyes were imaged with the combined SLO/OCT system, with one dataset excluded because the SLO data was not properly saved, thus, four effective paired datasets were analyzed. The overall retinal response can be measured by directly averaging image intensities. To minimize experimental variations, results were normalized to the base intensity, as shown in Figure 8 (a). In general, the SLO image intensities increased to 1.2 – 1.3 times their original values after the visible-light stimulus. The signal (i.e., the difference between the maximum ratio and the baseline) to noise (i.e., the standard deviation of the baseline) ratios (SNRs) were also calculated, and with the average SNR of the SLO signal determined to be ~16 (Table 2). The overall response can also be measured by averaging the OCT volumes, and the normalized OCT intensity changes before and after being subject to the stimulus are shown in Figure 8 (b). In contrast to the SLO results, the OCT signals were less noisy but had smaller absolute increase in intensity (0.10 for OCT vs. 0.24 for SLO), with an SNR value at ~8.6 times higher than that of SLO. Thus, measuring the retinal functional response with the averaged OCT volume is more accurate than using SLO to probe ORG scattering signals.

We further compared the timing of the averaged SLO and OCT signals. To facilitate comparison, the results were rescaled, with 0 assigned to the baseline value and 1 assigned to the maximum. As shown in Figure 8 (c), the signals were matched very well in the rising part, with a mean difference close to zero in the first 100s. During the falling part, in contrast, they were slightly mismatched with the mean difference marginally larger than zero, indicating a slower recovery for the SLO intensity than for the OCT intensity. Consider a simplified model of the imaging systems, as shown in Figure 8 (d). The SLO detector is nearly 3 times larger than the Airy disk of the imaging system and therefore it collects the back-reflected light at a small angle (indicated by both blue and red arrows), while the OCT detector, being similar in size to the system Airy disk and, when further combined with the coherent gate, collects only that light which is directly back-reflected by the sample (indicated by red arrows). Considering that the difference between the SLO and OCT signals changed between the rising and falling phases, it may indicate changes in the scattering

profile of the back-reflected light. Fpr example, the ratio between the light collected by SLO alone (blue arrows) and the light collected by both SLO and OCT (red arrows) was slightly different at these two stages.

4.2 Correlation between OCT line profile and the RPE anatomy

Regarding the RPE anatomy in this study: As aforementioned, B6 albino mice were used to visualize BrM. It is worth pointing out here that RPE presents differently between albino and pigmented mice in OCT images[31, 45]. BrM is visible in albino mice, but is not easily resolvable in pigmented mic due to the presence of melanosomes in the RPE containing highly scattering melanin pigment[46]. This strong signal from melanin obscures (or is convoluted within) the signal from the BrM in pigmented mice. The melanosomes are located at the apical side of the RPE, whereas the BrM is adjacent to the basolateral side of the RPE. The OS tips are adjacent to or juxtaposed on the apical RPE (microvilli interdigitation of the photoreceptor OS). Therefore, the deconvolution effectively resolved the photoreceptor OS tips from the apical RPE (Figure 3, OS tips and apical RPE). This assignment was confirmed in our previous work[32] in correlating OCT B-scan images with a high-resolution confocal microscopy image of a mouse retina plastic section.

The albino mice used in these studies are supposedly free of melanin. However, if no pigment is present, then how does one visualize the apical RPE? It could be hypothesized that albino mice still have melanosomes in their apical RPE and microvilli, but not in those with fully enzymatically converted melanin pigment granules. Thus, they still have some aspect of this highly scattering feature of melanin/melanosomes, but it is not as strong as that of a pigmented animal. This could also be attributed to the minor difference in the refractive index of RPE cell bodies and their upper surroundings. In essence, the first scattering peak adjacent to the BrM was labeled as the apical RPE, with everything between the apical RPE and BrM still considered to be the RPE even though it was a dark band with (what appeared to be) a space free of back-scatter. In contrast, the gap between the apical RPE and OS tips, namely the sub-retinal space (SRS), was barely resolved by deconvolution given the insufficient axial resolution of the SD-OCT system used in this work.

4.3 Diversity of the light induced functional ORG signals

As stated in the introduction, several works have, since 2006, used OCT to extract functional ORG signals. Earlier works focused on the scattering signals, and the photoreceptor elongation signals could be extracted only recently, owing to the advancements in OCT technology and data post-processing methods. The diversity of functional ORG signals of the retina is manifested in the following two aspects:

1. Within the same species, more and more functional signals are being revealed. For example, in our series of studies exploring the ORG signal of mice, the rod ISOS peak intensity scattering and position shifting were reported in the beginning[23], after which the the scattering signal from the apical side of RPE and RPE thickening were reported later[32]. In this study, the scattered ORG signal was also reported from the ONL. In human studies, changes in the optical path length of the cone OS were the first to be reported[13], followed by the potential signals

from Ganglion cells[47], RPE apical side position changes[15], and finally rod OS elongation[17, 21].

2. To compare the ORG signals between different species, one needs to consider the difference in their retinal morphology as well as the diurnal vs. nocturnal operation of their retinas. For example, in studies on nocturnal mice, the rod photoreceptor scattering and elongation signals were the most notable of all signals[23], while in studies involving humans (a diurnal specie), the cone OS elongation signals predominanted[17, 21]. In frog retina (nocturnal species), scattering intensity changes of both IS/OS[48] and RPE[49], were observed along with changes in the OS length[50, 51]. Although the SNRs of these signals are relatively low, as expected, there have also been similar reports of ORG signals from other species, such as, the tree shrew[52] and the macaque[53]. These have not been elaborated on here because of space constraints.

4.4 Limitations of modeling the retina response by second-order system

In this study, we used a second-order system to simulate retinal signals with an underlying assumption that attributed most of the retinal responses to mechanical changes in the retinal structures. While it did fit the measured ORG signal very well, there were still some discrepancies, especially in the recovery parts of the signals (e.g., Figures 4 (c) and 5 (f)). Given the high SNR of the measured signals, this mismatch cannot be attributed to noise. One possible reason is that: other processes, such as the changes in the local refractive index due to biochemical reactions or the activities performed by cell organelles, could also contribute to changing the optical signal and cause a mismatch between the measured data and its second-order fit. However, this requires further investigation in the future.

5 CONCLUSION

In conclusion, we proposed a method based on volumetric OCT data acquisition and analysis to study the retina. This method greatly increased the measurement accuracy of the functional ORG signals from the retina, enabled an analysis of its spatial properties, and revealed new features of different kinds of functional signals. In addition, blind deconvolution successfully deblurred the OCT averaged A-scan line profiles and recovered the OS tips and apical RPE across the volume, which was proven to be an effective way to increase the image quality to a reasonable extent. Finally, by applying this method, new signals representing different parts of the retina were discovered, demonstrating its capability as a powerful tool for extracting weak functional signals at high SNR values. This leaves two directions of research open for investigation in future studies: (1) increasing the data acquisition speed to increase the temporal resolution of the method to probe faster signals; (2) increasing the data post-processing speed to accelerate signal processing, and make it convenient for use in routine screening to study the retinal function alterations associated with aging, trans-genetic modification, disease or treatment of rodent eyes.

ACKNOWLEDGMENTS

We sincerely thank Dr. Edward N. Pugh Jr. at the UC Davis for the valuable help. We sincerely thank Dr. Dezong Zhao of the University of Glasgow for aiding us with a discussion of the second-order system. This research was

supported by funding from Dalian University of Technology (DUT21RC(3)001 & DUT21YG121) (P.Z.) and the National Natural Science Foundation of China (Grant No. 62175024 (P.Z.)). This work was also supported by NIH EY026556 (RJZ), NIH EY031098 (RJZ), and the UC Davis NEI Vision Center Core Grant NIH EY012576 (RJZ).

DATA AVAILABILITY STATEMENT

Research data are not shared.

Abbreviations:

OCT	optical coherence tomography
3D	three-dimensional

REFERENCES

[1]. Hildebrand GD, Fielder AR in Anatomy and Physiology of the Retina, Vol. (Eds.: Reynolds J, Olitsky S), Springer Berlin Heidelberg, Berlin, Heidelberg, 2011, pp. 39–65.

[2]. Liebman PA, Jagger WS, Kaplan MW, Bargoot FG Nature 1974, 251, 31–36. [PubMed: 4547251]

[3]. Harary H, Brown J, Pinto L Science 1978, 202, 1083–1085. [PubMed: 102035]

[4]. Huang D, Swanson E, Lin C, Schuman J, Stinson W, Chang W, Hee M, Flotte T, Gregory K, Puliafito C, a. et Science 1991, 254, 1178–1181. [PubMed: 1957169]

[5]. Yao X-C, Yamauchi A, Perry B, George JS Appl. Opt 2005, 44, 2019–2023. [PubMed: 15835350]

[6]. Bizheva K, Pflug R, Hermann B, Považay B, Sattmann H, Qiu P, Anger E, Reitsamer H, Popov S, Taylor JR, Unterhuber A, Ahnelt P, Drexler W Proc Natl Acad Sci U S A 2006, 103, 5066–5071. [PubMed: 16551749]

[7]. Srinivasan VJ, Wojtkowski M, Fujimoto JG, Duker JS Opt. Lett 2006, 31, 2308–2310. [PubMed: 16832468]

[8]. Jonnal RS, Rha J, Zhang Y, Cense B, Gao W, Miller DT Opt. Express 2007, 15, 16141–16160.

[9]. Srinivasan VJ, Chen Y, Duker JS, Fujimoto JG Opt. Express 2009, 17, 3861–3877. [PubMed: 19259228]

[10]. Tumlinson AR, Hermann B, Hofer B, Považay B, Margrain TH, Binns AM, Drexler W Japanese Journal of Ophthalmology 2009, 53, 315–326. [PubMed: 19763748]

[11]. Zhang Q, Lu R, Wang B, Messinger JD, Curcio CA, Yao X Scientific Reports 2015, 5, 9595. [PubMed: 25901915]

[12]. Yao X-C, Zhao Y-B Opt. Express 2008, 16, 12446–12459. [PubMed: 18711481]

[13]. Hillmann D, Spahr H, Pfäffle C, Sudkamp H, Franke G, Hüttmann G Proc Natl Acad Sci U S A 2016, 113, 13138–13143. [PubMed: 27729536]

[14]. Spahr H, Pfäffle C, Burhan S, Kutzner L, Hilge F, Hüttmann G, Hillmann D Sci Rep 2019, 9, 11748. [PubMed: 31409819]

[15]. Azimipour M, Migacz JV, Zawadzki RJ, Werner JS, Jonnal RS Optica 2019, 6, 300–303. [PubMed: 33511257]

[16]. Zhang F, Kurokawa K, Lassoued A, Crowell JA, Miller DT Proc Natl Acad Sci U S A 2019, 116, 7951–7956. [PubMed: 30944223]

[17]. Azimipour M, Valente D, Vienola KV, Werner JS, Zawadzki RJ, Jonnal RS Opt. Lett 2020, 45, 4658–4661. [PubMed: 32870829]

[18]. Pandiyan VP, Jiang X, Maloney-Bertelli A, Kuchenbecker JA, Sharma U, Sabesan R Biomed. Opt. Express 2020, 11, 5274–5296. [PubMed: 33014614]

[19]. Pandiyan VP, Maloney-Bertelli A, Kuchenbecker JA, Boyle KC, Ling T, Chen ZC, Park BH, Roorda A, Palanker D, Sabesan R Science Advances 2020, 6, eabc1124. [PubMed: 32917686]

[20]. Boyle KC, Chen ZC, Ling T, Pandiyan VP, Kuchenbecker J, Sabesan R, Palanker D Biophysical Journal 2020, 119, 1481–1488. [PubMed: 33031739]

[21]. Lu CD, Lee B, Schottenhamml J, Maier A, Pugh EN Jr., Fujimoto JG Invest Ophthalmol Vis Sci 2017, 58, 4632–4643. [PubMed: 28898357]

[22]. Ma G, Son T, Kim T-H, Yao X Biomed. Opt. Express 2021, 12, 2661–2669. [PubMed: 34123495]

[23]. Zhang P, Zawadzki RJ, Goswami M, Nguyen PT, Yarov-Yarovoy V, Burns ME, Pugh EN Jr. Proc Natl Acad Sci U S A 2017, 114, E2937–E2946. [PubMed: 28320964]

[24]. Schmidt FL, Hunter JE Intelligence 1999, 27, 183–198.

[25]. Liu Z, Kurokawa K, Zhang F, Lee JJ, Miller DT Proceedings of the National Academy of Sciences 2017, 114, 12803–12808.

[26]. Hammer DX, Agrawal A, Villanueva R, Saeedi O, Liu Z Proceedings of the National Academy of Sciences 2020, 117, 30661–30669.

[27]. Zhang P, Miller EB, Manna SK, Meleppat RK, Pugh EN Jr., Zawadzki RJ Neurophotonics 2019, 6, 041105. [PubMed: 31528657]

[28]. Pi S, Hormel TT, Wei X, Cepurna W, Morrison JC, Jia Y Opt. Lett 2020, 45, 2107–2110. [PubMed: 32236080]

[29]. Miller EB, Zhang P, Ching K, Pugh EN Jr., Burns ME Proc Natl Acad Sci U S A 2019, 116, 16603–16612. [PubMed: 31350349]

[30]. Zhang P, Zam A, Jian Y, Wang X, Li Y, Lam KS, Burns ME, Sarunic MV, Pugh EN Jr., Zawadzki RJ J Biomed Opt 2015, 20, 126005. [PubMed: 26677070]

[31]. Zhang P, Goswami M, Zawadzki RJ, Pugh EN Jr. Invest Ophthalmol Vis Sci 2016, 57, 3650–3664. [PubMed: 27403994]

[32]. Zhang P, Shibata B, Peinado G, Zawadzki RJ, FitzGerald P, Pugh EN Jr Investigative Ophthalmology & Visual Science 2020, 61, 9–9.

[33]. Ni S, Wei X, Ng R, Ostmo S, Chiang MF, Huang D, Jia Y, Campbell JP, Jian Y Biomed. Opt. Express 2021, 12, 3553–3570. [PubMed: 34221678]

[34]. Levin A, Weiss Y, Durand F, Freeman WT in Understanding and evaluating blind deconvolution algorithms, Vol. (Ed.Êds.: Editor), City, 2009, pp. 1964–1971.

[35]. Zhang P, Mocci J, Wahl DJ, Meleppat RK, Manna SK, Quintavalla M, Muradore R, Sarunic MV, Bonora S, Pugh EN, Zawadzki RJ Experimental Eye Research 2018, 172, 86–93. [PubMed: 29604280]

[36]. Omri S, Omri B, Savoldelli M, Jonet L, Thillaye-Goldenberg B, Thuret G, Gain P, Jeanny JC, Crisanti P, Behar-Cohen F Clin Ophthalmol 2010, 4, 183–195. [PubMed: 20463783]

[37]. Zhang P, Goswami M, Zam A, Pugh EN, Zawadzki RJ Opt. Lett 2015, 40, 5830–5833. [PubMed: 26670523]

[38]. Muir ER, Duong TQ NMR in Biomedicine 2011, 24, 216–223. [PubMed: 20821409]

[39]. Cone FE, Steinhart MR, Oglesby EN, Kalesnykas G, Pease ME, Quigley HA Experimental Eye Research 2012, 99, 27–35. [PubMed: 22554836]

[40]. Ding C, Wang P, Tian N Experimental Eye Research 2011, 92, 512–520. [PubMed: 21457709]

[41]. Nair G, Kim M, Nagaoka T, Olson DE, Thulé PM, Pardue MT, Duong TQ Documenta Ophthalmologica 2011, 122, 163–176. [PubMed: 21519880]

[42]. Helmstaedter M, Briggman KL, Turaga SC, Jain V, Seung HS, Denk W Nature 2013, 500, 168–174. [PubMed: 23925239]

[43]. Son T, Alam M, Toslak D, Wang B, Lu Y, Yao X Journal of Biophotonics 2018, 11, e201800089. [PubMed: 29770594]

[44]. Cunha-Vaz J, Mechanisms of Retinal Fluid Accumulation and Blood-Retinal Barrier Breakdown, Dev Ophthalmol. , Basel, 2017.

[45]. Zhang T, Kho AM, Zawadzki RJ, Jonnal RS, Yiu G, Srinivasan VJ Opt. Lett 2020, 45, 5945–5948. [PubMed: 33137037]

[46]. Song W, Zhang L, Ness S, Yi J Biomed. Opt. Express 2017, 8, 3966–3980. [PubMed: 29026682]

[47]. Pfäffle C, Spahr H, Kutzner L, Burhan S, Hilge F, Miura Y, Hüttmann G, Hillmann D Opt. Lett 2019, 44, 5671–5674. [PubMed: 31774751]

[48]. Lu R-W, Zhang Q-X, Yao X, Curcio C, Zhang Y, Pittler S, Deretic D Journal of Biomedical Optics 2012, 17, 060504. [PubMed: 22734727]

[49]. Zhang Q-X, Lu R-W, Messinger JD, Curcio CA, Guarcello V, Yao X-C Scientific Reports 2013, 3, 2644. [PubMed: 24025778]

[50]. Zhao X, Thapa D, Wang B, Lu Y, Gai S, Yao X Journal of Biomedical Optics 2016, 21, 065006.

[51]. Lu Y, Benedetti J, Yao X Translational Vision Science & Technology 2018, 7, 29–29.

[52]. Erchova I, Tumlinson AR, Fergusson J, White N, Drexler W, Sengpiel F, Morgan JE Scientific Reports 2018, 8, 1813. [PubMed: 29379036]

[53]. Suzuki W, Tsunoda K, Hanazono G, Tanifuji M Investigative Ophthalmology & Visual Science 2013, 54, 6345–6354. [PubMed: 23982841]

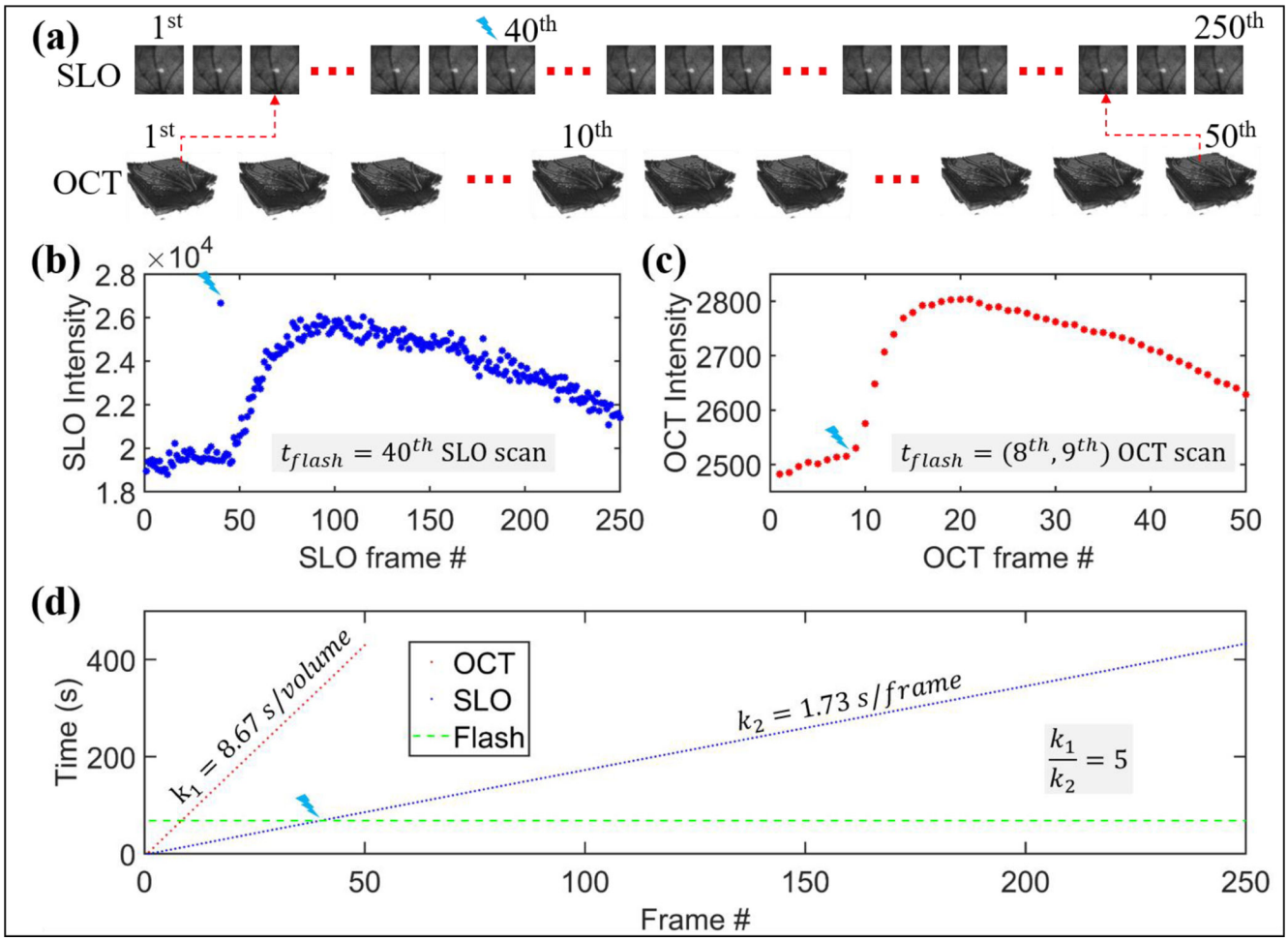

Figure 1.

SLO and OCT data acquisition protocols and timings. (a) The SLO frame and OCT volume were acquired simultaneously, but at different time intervals. Note that the bleaching flash was delivered during the 40th SLO frame, which was between the 8th and 9th OCT volumes; (b) the outlier data point is caused by the bleaching light detected by the SLO detector. (b, c) The overall SLO and OCT intensities were monitored before and after the flash, respectively. (d) The timing of the SLO and OCT imaging, and the flashlight; the red and blue dotted lines represent the timing of OCT volumes and SLO frames, while the green dashed line represents the bleaching flash associated with the 40th SLO scan.

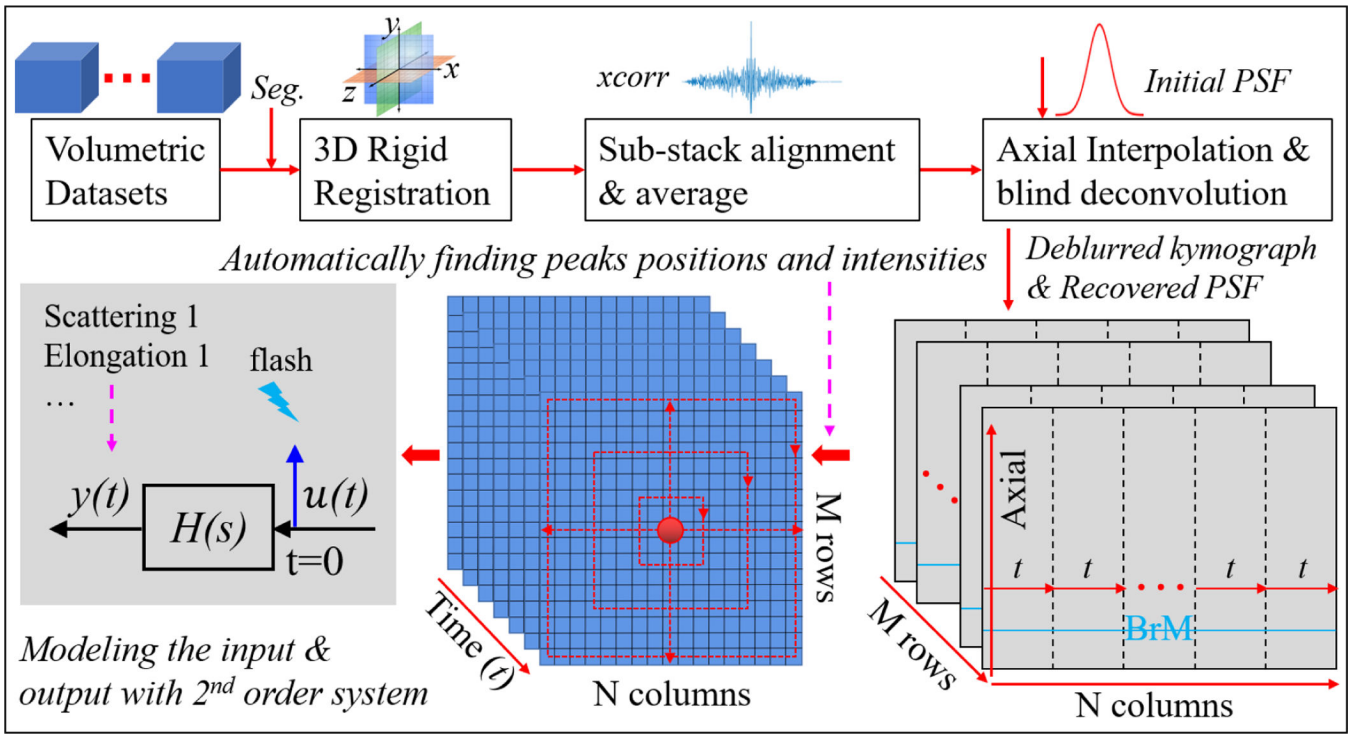

Figure 2.

Data processing steps: The volumetric OCT datasets were first aligned by a 3D rigid registration apporach[27] with segmented (Seg.) *enface* images as one input. The data were then divided into sub-stacks, each containing 20 × 20 A-scans taken in the lateral and vertical directions, respectively. The sub-stacks were first aligned by cross-correlation[32], then averaged, and finally axially interpolated to 0.1μm/pixel and deconvoluted by the blind deconvolution algorithm. The peak intensities and their positions were then automatically detected and recorded for further modeling with the second-order system.

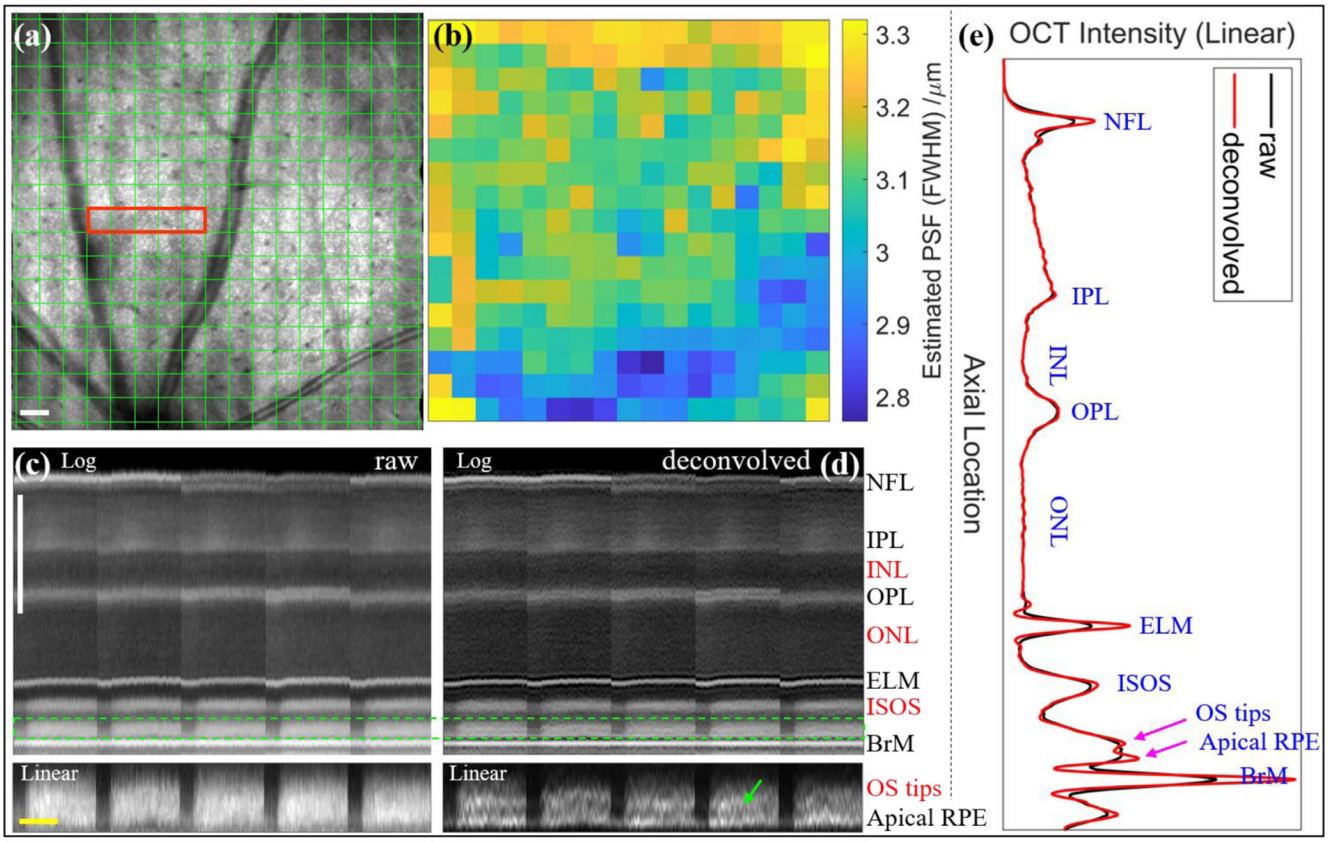

Figure 3.

Blind deconvolution on the functional OCT data. (a) Green lattice, projected on an averaged OCT enface image. (b) Estimated axial PSF for each block in the lattice. (c, d) The raw and deconvolved kymogram of the data in the middle row of the lattice (red rectangle in (a)). The upper parts were displayed on a logarithmic scale to help visualize all the layers, while the lower parts were displayed on a linear scale to highlight the dark band which separated OS tips and apical RPE. (e) Comparison between the raw and deconvolved line profiles. Abbreviations: NFL – Nerve Fiber Layer, IPL – Inner Plexiform Layer, INL – Inner Nuclear Layer, ONL – Outer Nuclear Layer, OPL – Outer Plexiform Layer, ELM – External Limiting Membrane, ISOS – Inner Segment / Outer Segment, OS tips – Outer Segment Tips, RPE - Retinal Pigment Epithelium, BrM – Bruch's Membrane. Scale bars: (white) 100 μm, (yellow) 200 s.

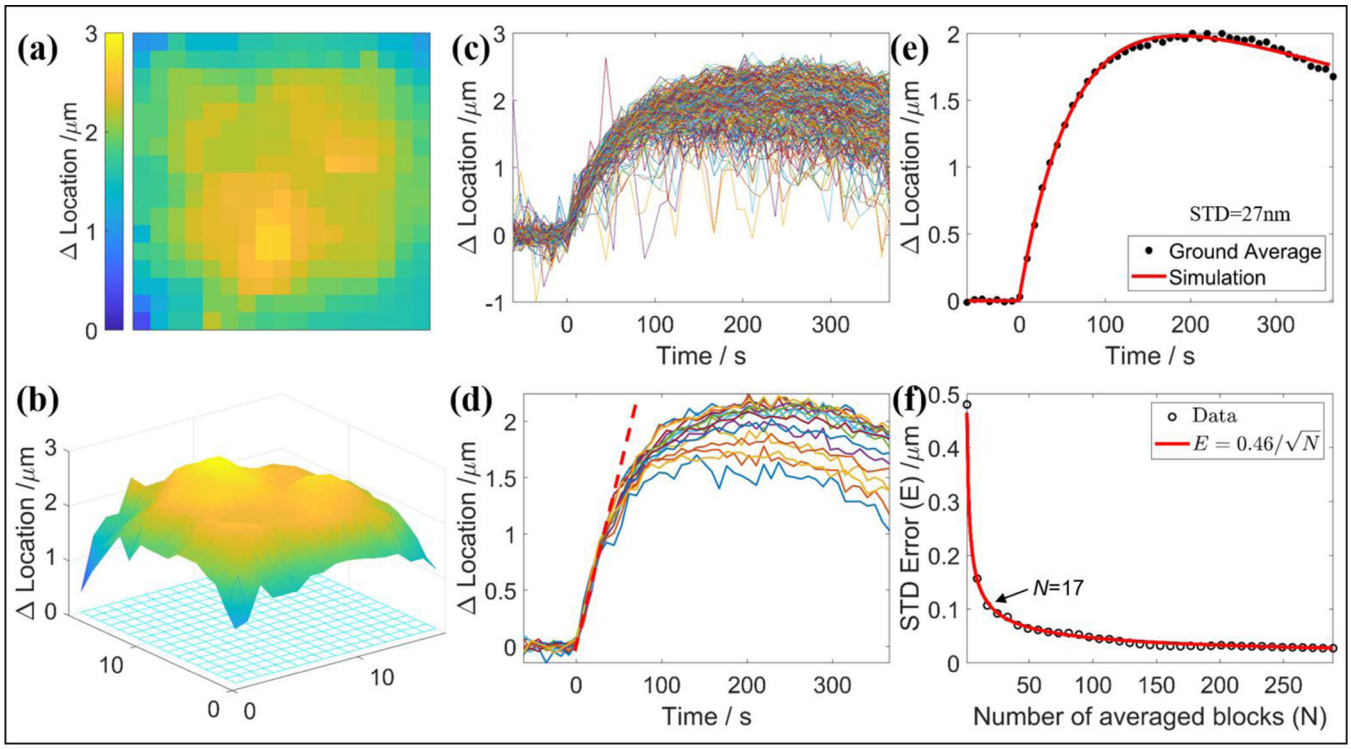

Figure 4.

Spatially-resolved, functional ORG signals, as extracted from the ELM peak position shifts. (a) *Enface* display of ELM peak location changes (relative to BrM) at its maximum response. (b) The 3D display of (a). (c) Raw signal from all the individual blocks in the lattice. (d) Averaged signal from each lattice row. Red dashed line indicates the near-identical initial slope of all signals at the first ~30 s after bleaching. (e) Overall averaged signal and its fit with a second-order system transfer function. (f) Variation in standard error with the number of averaged blocks.

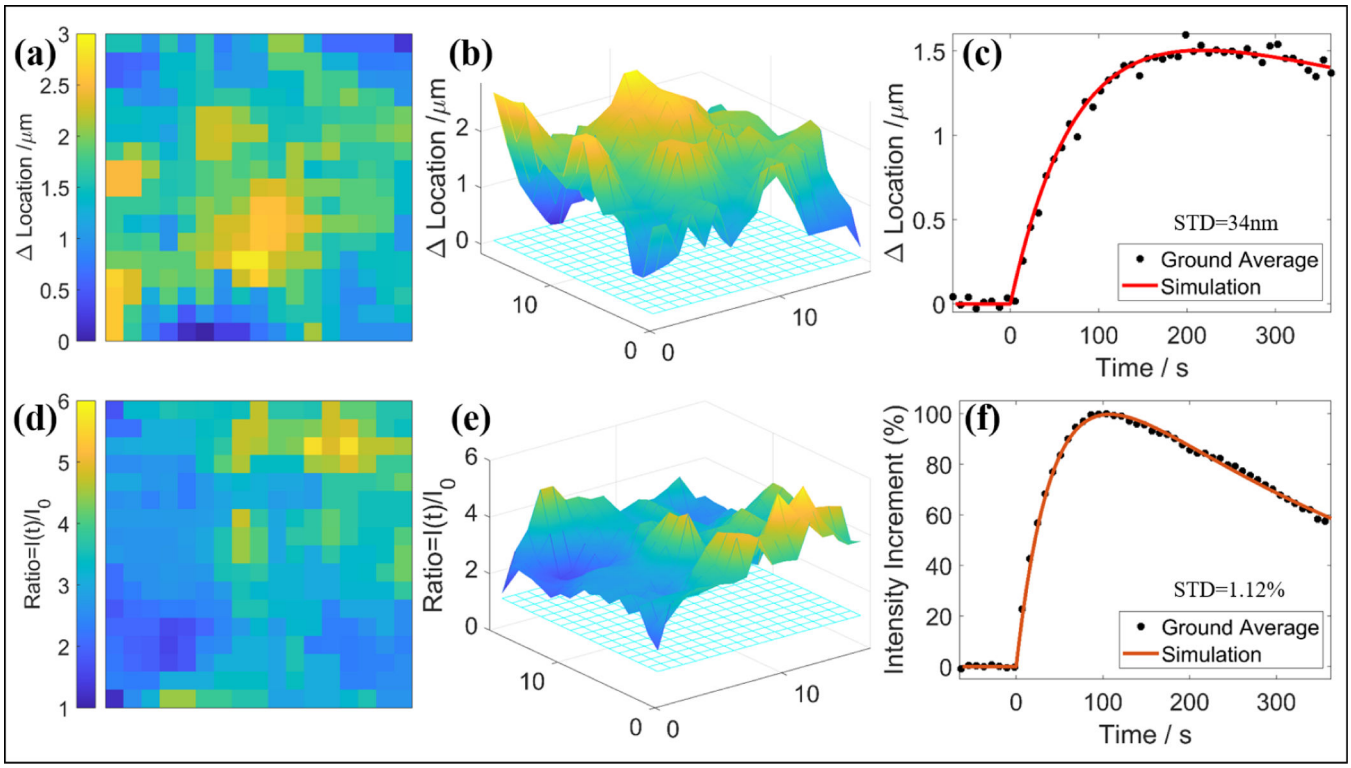

Figure 5.

Spatially-resolved functional signals from the peak location and intensity of ISOS. (a, d) *Enface* displays of the ISOS peak location and intensity at their maximum responses. (b, e) 3D display of (a) and (d), respectively. (c, f) Overall averaged signals for (a) and (d) and their fit with second-order system transfer functions. Note that: in panels (d) and (e), I(t) represents the intensity at the time of maximum ISOS scattering response, while I_0 represents the dark-adapted ISOS scattering intensity.

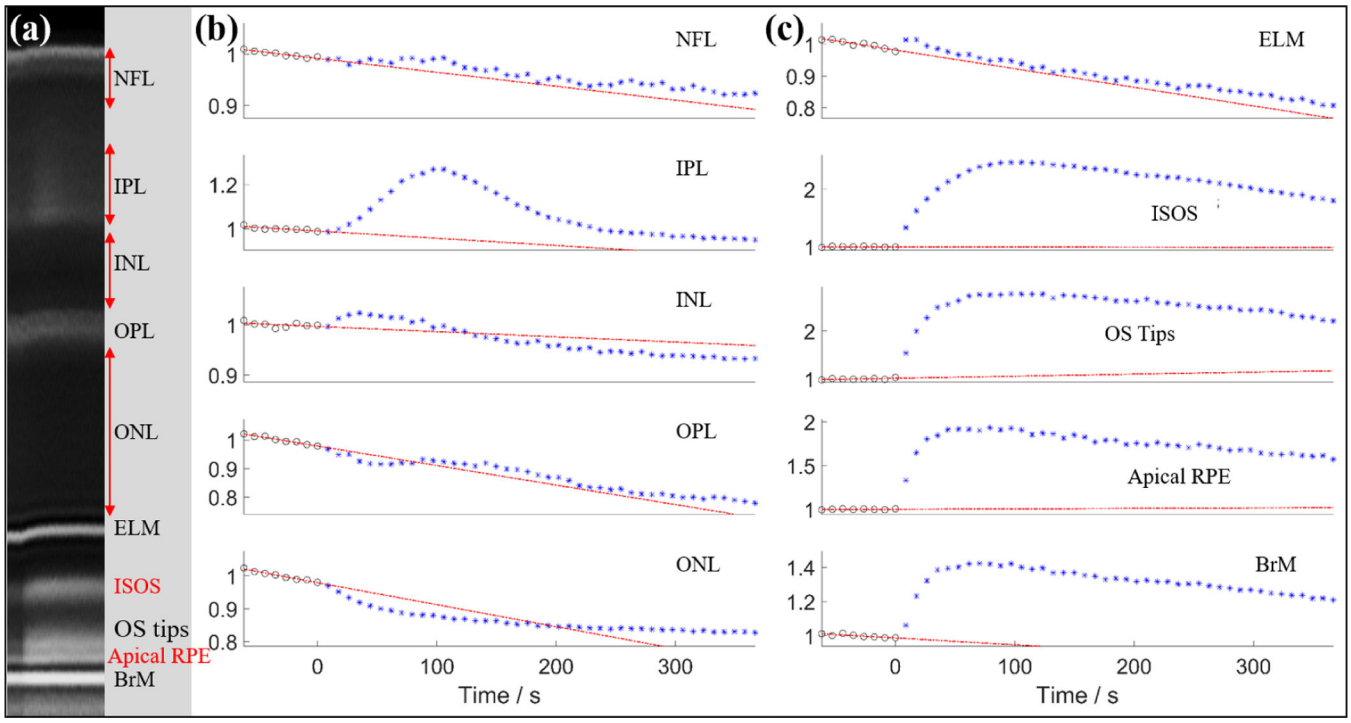

Figure 6.

The overall averaged scattering signals from ten different retinal bands, ranging from NFL to BrM. Black dots and blue stars denote the data before and after bleaching, respectively, while the red, dashed lines represent the least-square linear fit with the pre-bleaching data to depict the changing trend of the dark-adapted retina.

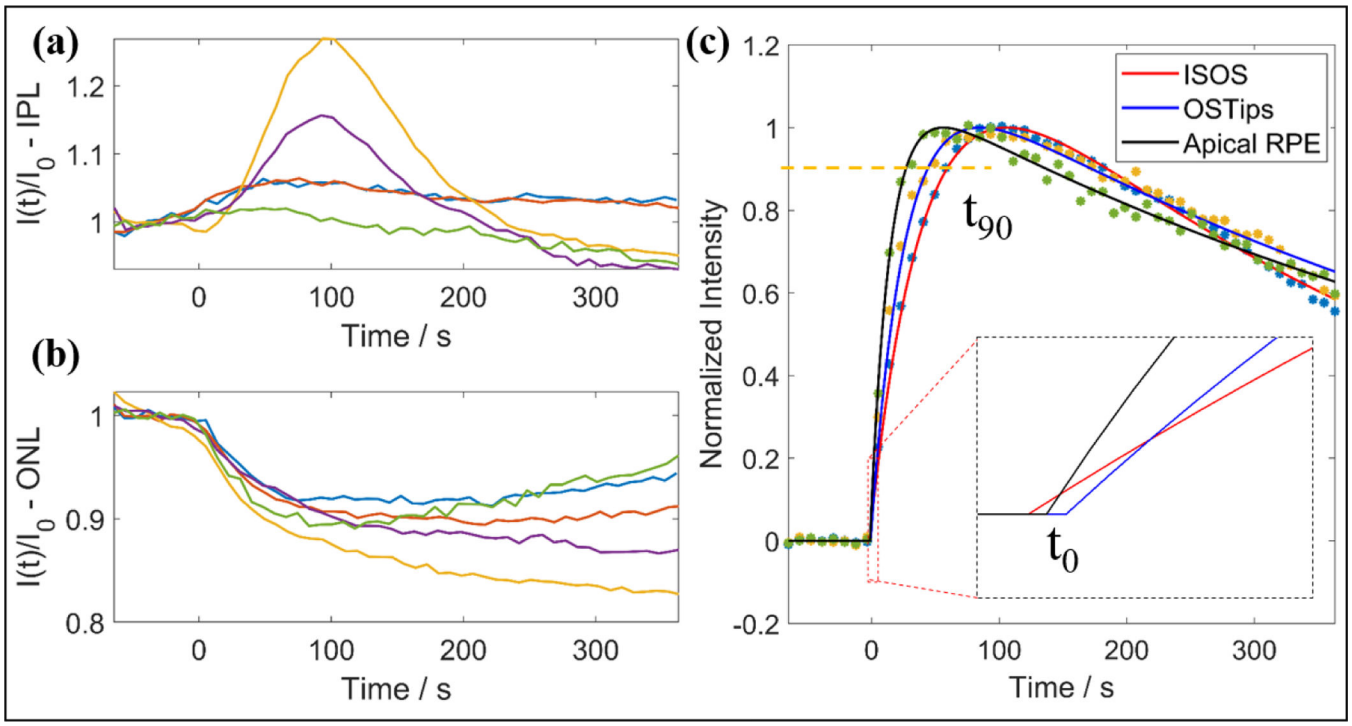

Figure 7.

The novel functional signals resolved by the volume averaging method. (a, b) Variations in IPL and ONL peak intensity ratio for the five pairs of mouse eyes. (c) Normalized and re-scaled (minimum to 0 and maximum to 1) scattering intensity of ISOS, OS tips and RPE data. Their starting times (t_0) and changing speeds (t_{90}) were extracted from the second-order system fit to the data. Note that: in panels (a) and (b), I(t) represents the signal intensity at different time points, while I_0 represents the average dark-adapted scattering intensity.

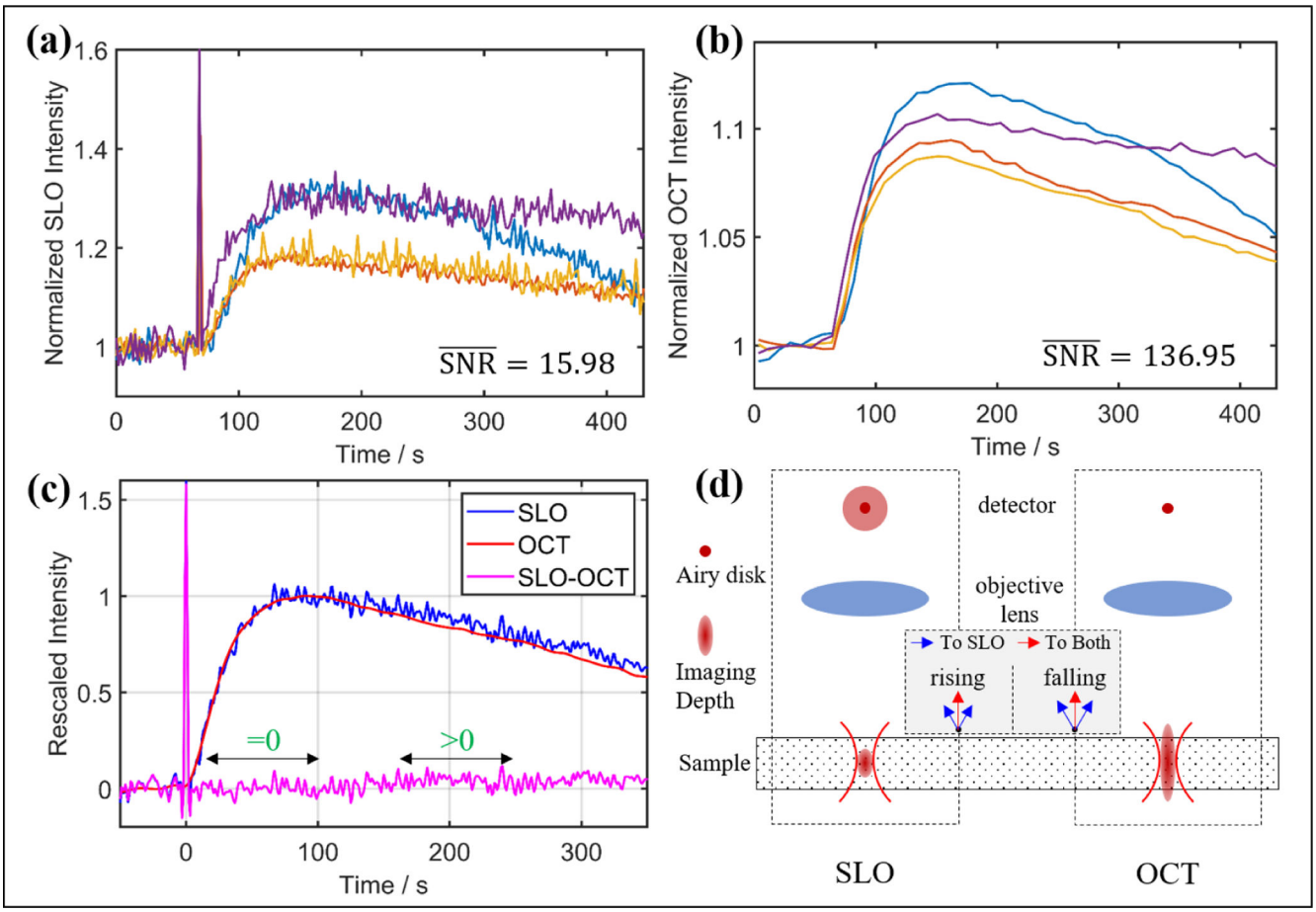

Figure 8.

Overall light induced changes in retinal scattering as the functional signals were extracted from the SLO and OCT data. (a) Retinal scattering intensities, measured by averaging SLO frames. (b) Retinal scattering intensities, measured by averaging OCT volumes. (c) Comparison of the normalized ORG signals from SLO and OCT. (d) Schematic depicting the back-reflected light collected by SLO and OCT. Note that: the jump in intensity increase at t=0, represented by the outlier dot in panels (a) and (c), is attributed to the SLO capturing both the bleaching and the imaging lights (488nm & 860nm, respectively). SLO intensities at all other time points were generated by the NIR imaging light (860nm) alone.

TABLE 1.

The starting time (t_0) after light stimulus and the time taken to attain 90% signal intensity (t_{90}) extracted from the second-order system fit for ISOS, OS tips, and apical RPE data.

Layer	t_0 (s)					AVG	t_{90} (s)					AVG
ISOS	1.15	0	0.03	0	1.22	0.48	52	58	61	56	56	56.6
	10 × noise					0.80						55.8
OS tips	0	2.62	0	0.26	0	**0.58**	57	62	46	48	49	**52.4**
	10 × noise					1.24						54.0
Apical RPE	1.28	2.04	1.67	2.38	1.29	**1.73**	40	53	29	34	27	**36.6**
	10 × noise					1.79						36.0

TABLE 2.

SNR attributes of the ORG functional signals measured by SLO and OCT.

	SLO (Figure 8 (a))				OCT (Figure 8 (b))			
Signal[a)]	0.317	0.177	0.186	0.296	0.121	0.095	0.087	0.105
Noise[b)]	0.0147	0.0096	0.0170	0.0227	0.0014	4.4e-4	5.3e-4	0.0013
SNR	21.6	18.4	10.9	13.0	86.4	217.4	163.2	80.8

*a)*The signal is defined as the maximum response of the functional signal;

*b)*The noise is defined as the standard deviation of the dark-adapted retinal scattering intensity.